

1 **First-principles transport calculation method based on real-space**
 2 **finite-difference nonequilibrium Green's function scheme**

3 Tomoya Ono¹, Yoshiyuki Egami², and Kikuji Hirose¹

4 ¹*Graduate School of Engineering, Osaka University, Suita, Osaka 565-0871, Japan*

5 ²*Nagasaki University Advanced Computing Center,*

6 *Nagasaki University, Bunkyo-machi, Nagasaki 852-8521, Japan*

7 (Dated: May 18, 2018)

Abstract

We demonstrate an efficient nonequilibrium Green's function transport calculation procedure based on the real-space finite-difference method. The direct inversion of matrices for obtaining the self-energy terms of electrodes is computationally demanding in the real-space method because the matrix dimension corresponds to the number of grid points in the unit cell of electrodes, which is much larger than that of sites in the tight-binding approach. The procedure using the ratio matrices of the overbridging boundary-matching technique [Phys. Rev. B **67**, 195315 (2003)], which is related to the wave functions of a couple of grid planes in the matching regions, greatly reduces the computational effort to calculate self-energy terms without losing mathematical strictness. In addition, the present procedure saves computational time to obtain Green's function of the semi-infinite system required in the Landauer-Büttiker formula. Moreover, the compact expression to relate Green's functions and scattering wave functions, which provide a real-space picture of the scattering process, is introduced. An example of the calculated results is given for the transport property of the BN ring connected to (9,0) carbon nanotubes. The wave function matching at the interface reveals that the rotational symmetry of wave functions with respect to the tube axis plays an important role in electron transport. Since the states coming from and going to electrodes show threefold rotational symmetry, the states in the vicinity of the Fermi level, whose wave function exhibits fivefold symmetry, do not contribute to the electron transport through the BN ring.

8 PACS numbers: 71.15.-m, 72.10.-d, 72.80.Rj, 73.40.-c

9 I. INTRODUCTION

10 Recently, electronic-structure calculations have become an important tool for investigat-
11 ing the physics and chemistry of nanoscale systems with the miniaturization of electronic
12 devices. The electron-transport properties of nanoscale systems have been studied actively
13 because they are of significant importance from both fundamental and practical points of
14 view. Owing to the complexity of the problem, such studies are strongly dependent on the
15 existence of reliable numerical treatments based on first-principles approaches.

16 A number of first-principles calculation methods for the electron-transport properties of
17 nanoscale systems have been proposed so far. They are roughly categorized into two ap-
18 proaches. One approach uses the nonequilibrium Green's function (NEGF). The relation be-
19 tween conductance and Green's function has been derived within the nonequilibrium Keldysh
20 formalism.¹ This approach has been used extensively in connection with tight-binding mod-
21 els and first-principles methods employing localized basis sets consisting of either atomic
22 orbitals²⁻⁴ or Gaussians.⁵ In this formalism, by making use of Green's functions with en-
23 ergies of nonreal numbers, the electronic structures of the isolated states in the transition
24 region, which are not easily treated only by the energies of real numbers, can be included into
25 the total charge density of the system. On the other hand, the NEGF method has not been
26 employed with the real-space⁶⁻⁸ and plane-wave formalisms so far because the large num-
27 bers of grid points or plane waves prevent the direct inversion of $N_x \times N_y \times N_z$ -dimensional
28 matrices to obtain the surface Green's functions and self-energy terms of electrodes, where
29 N_x , N_y , and N_z are the numbers of grid points along the x -, y -, and z -directions in the unit
30 cell of the left or right electrode and electrons flow along the z -direction [see, e.g., Fig. 1].

31 The other approach is to compute the scattering wave functions from which transmission
32 coefficients can be obtained. In addition, the scattering wave functions provide a direct
33 real-space picture of the scattering process. This approach has been employed by combining
34 it with techniques where real-space grids and/or plane wave basis sets⁸⁻¹⁴ are used to de-
35 scribe wave functions and potentials. The easiest way to obtain scattering wave functions is
36 to solve the Lippman-Schwinger equation where the semi-infinite electrode is replaced with
37 a uniformly distributed charge background, i.e., "jellium."⁹ The scattering wave function
38 can alternatively be calculated by the wave-function-matching approach proposed by Fuji-
39 moto and Hirose, i.e., the overbridging boundary-matching (OBM) method.^{8,14} In the OBM

40 method, several parts of Green's functions of the transition region are computed to set up
41 the wave-function-matching formula and there is no limitation of the usage of jellium, i.e.,
42 more realistic atomic and electronic structures of the electrode can be taken into account.
43 Moreover, the effect of electrodes is included in the matching formula as $N_x \times N_y \times \mathcal{N}_f$ -
44 dimensional ratio matrices, where \mathcal{N}_f is the order of the finite-difference approximation⁶ for
45 the kinetic energy operator in the Kohn-Sham equation and is much smaller than N_z .

46 In this paper, we propose the real-space finite-difference (RSFD) NEGF scheme and
47 demonstrate that the surface Green's functions and self-energy terms of the electrodes re-
48 quired in the NEGF method can be obtained from the ratio matrices in the OBM method.
49 The dimension of the matrices for the surface Green's functions and self-energy terms that
50 are directly inverted is reduced from $N_x \times N_y \times N_z$ to $N_x \times N_y \times \mathcal{N}_f$ in the present scheme while
51 keeping the rigorousness of the mathematical formulation. This advantage also saves com-
52 putational effort to calculate Green's functions in the transition region because the number
53 of elements of the Green's-function matrix required for the transport calculation is propor-
54 tional to the dimension of the matrices of the self-energy terms. In addition, we prove that
55 scattering wave functions, which help us to interpret the scattering process and are usually
56 calculated by wave function matching methods, can be obtained within the framework of
57 the RSFD NEGF method.

58 The rest of this paper is organized as follows: in Sec. II, we relate the important quan-
59 tities of the NEGF method to those of the OBM scheme, and introduce the RSFD NEGF
60 method. In Sec. III, we present an example showing that scattering wave functions help
61 us to interpret the scattering process by computing the transport properties of a BN ring
62 sandwiched between carbon nanotube electrodes (C/BNNT). In Sec. IV, we summarize our
63 procedures. Finally, a mathematical proof is given in appendix.

64 **II. NEGF METHOD USING THE COMPUTATIONAL PROCEDURE OF THE**
65 **OBM METHOD**

66 **A. Green's function of a whole system including the transition region and two**
67 **semi-infinite electrodes**

68 Let us consider Green's function of a system composed of the transition region sandwiched
69 between two semi-infinite crystalline electrodes, as shown in Fig. 1, within the framework of
70 the RSFD scheme. Two-dimensional periodicity in the x - and y -directions is assumed and a
71 generalized z -coordinate ζ_l instead of z_l is used, because a couple of grid planes are involved
72 in wave-function and Green's-function matching when higher-order finite-difference approx-
73 imation is employed (see Fig. 1). The exchange-correlation effect is treated by the local
74 density approximation¹⁵ or generalized gradient approximation¹⁶ of the density functional
75 theory.^{17,18}

76 The Green's-function matrix involves the inversion of an infinite matrix corresponding to
77 the Hamiltonian matrix of the whole system $\hat{H}(\mathbf{k}_{||})$, where $\mathbf{k}_{||}$ is the lateral Bloch vector.
78 As shown in Fig. 2, we are, however, interested in the finite part of the Green's-function
79 matrix,

$$\hat{H}(\mathbf{k}_{||}) = \left[\begin{array}{c|c|c} \hat{H}_L(\mathbf{k}_{||}) & \hat{B}_{LT} & 0 \\ \hline \hat{B}_{LT}^\dagger & \hat{H}_T(\mathbf{k}_{||}) & \hat{B}_{TR} \\ \hline 0 & \hat{B}_{TR}^\dagger & \hat{H}_R(\mathbf{k}_{||}) \end{array} \right], \quad (1)$$

80 where the borders of the partitioning of $\hat{H}(\mathbf{k}_{||})$ are drawn according to the dashed lines in
81 Fig. 1; the submatrix $\hat{H}_T(\mathbf{k}_{||})$ contains the matrix elements in the transition region, $\hat{H}_L(\mathbf{k}_{||})$
82 ($\hat{H}_R(\mathbf{k}_{||})$) corresponds to the semi-infinite left (right)-electrode region, and \hat{B}_{LT} (\hat{B}_{TR}), which
83 is nonzero only for some connection area between the transition region and the left (right)
84 electrode, is the interaction between the transition region and the electrodes. $\hat{H}_T(\mathbf{k}_{||})$ in the
85 transition region is treated as a general nonsparse matrix here and in subsequent subsections.
86 On the other hand, $\hat{H}_L(\mathbf{k}_{||})$ ($\hat{H}_R(\mathbf{k}_{||})$) is a block tridiagonal matrix in the RSFD formalism, all
87 of the block-matrix elements of which are $N(= N_x \times N_y \times \mathcal{N}_f)$ dimensional. In addition, \hat{B}_{LT}
88 (\hat{B}_{TR}) is a zero matrix except for one N -dimensional block-matrix element $B(\zeta_{-1})$ ($B(\zeta_{m+1})$),
89 as illustrated in Fig. 2. In practice, \mathcal{N}_f corresponds to the number of x - y grid planes involved
90 in the function-matching region ζ_l since the order of the finite-difference approximation is

91 chosen so as to include the nonlocal region of pseudopotentials in the matching region¹⁹ as
 92 well as to obtain sufficiently accurate results with the used grid spacing.

93 Green's function of the whole system is defined as

$$\begin{aligned}\hat{G}(Z, \mathbf{k}_{||}) &= [Z - \hat{H}(\mathbf{k}_{||})]^{-1} \\ &= \begin{bmatrix} \hat{G}_L(Z, \mathbf{k}_{||}) & \hat{G}_{LT}(Z, \mathbf{k}_{||}) & \hat{G}_{LR}(Z, \mathbf{k}_{||}) \\ \hat{G}_{TL}(Z, \mathbf{k}_{||}) & \hat{G}_T(Z, \mathbf{k}_{||}) & \hat{G}_{TR}(Z, \mathbf{k}_{||}) \\ \hat{G}_{RL}(Z, \mathbf{k}_{||}) & \hat{G}_{RT}(Z, \mathbf{k}_{||}) & \hat{G}_R(Z, \mathbf{k}_{||}) \end{bmatrix},\end{aligned}\quad (2)$$

94 where $Z(= E + i\eta)$ is a complex energy variable. From the matrix equation

$$\begin{bmatrix} Z - \hat{H}_L(\mathbf{k}_{||}) & -\hat{B}_{LT} & 0 \\ -\hat{B}_{LT}^\dagger & Z - \hat{H}_T(\mathbf{k}_{||}) & -\hat{B}_{TR} \\ 0 & -\hat{B}_{TR}^\dagger & Z - \hat{H}_R(\mathbf{k}_{||}) \end{bmatrix} \begin{bmatrix} \hat{G}_{LT}(Z, \mathbf{k}_{||}) \\ \hat{G}_T(Z, \mathbf{k}_{||}) \\ \hat{G}_{RT}(Z, \mathbf{k}_{||}) \end{bmatrix} = \begin{bmatrix} 0 \\ I \\ 0 \end{bmatrix},\quad (3)$$

95 that is,

$$\begin{aligned}\hat{G}_{LT}(Z, \mathbf{k}_{||})\hat{G}_T(Z, \mathbf{k}_{||})^{-1} &= [Z - \hat{H}_L(\mathbf{k}_{||})]^{-1} \hat{B}_{LT} \\ -\hat{B}_{LT}^\dagger \hat{G}_{LT}(Z, \mathbf{k}_{||}) + [Z - \hat{H}_T(\mathbf{k}_{||})] \hat{G}_T(Z, \mathbf{k}_{||}) - \hat{B}_{TR} \hat{G}_{RT}(Z, \mathbf{k}_{||}) &= I \\ \hat{G}_{RT}(Z, \mathbf{k}_{||})\hat{G}_T(Z, \mathbf{k}_{||})^{-1} &= [Z - \hat{H}_R(\mathbf{k}_{||})]^{-1} \hat{B}_{TR}^\dagger,\end{aligned}\quad (4)$$

96 one sees that Green's function of the whole system $\hat{G}_T(Z, \mathbf{k}_{||})$ can be partitioned to the
 97 transition region as

$$\hat{G}_T(Z, \mathbf{k}_{||}) = [Z - \hat{H}_T(\mathbf{k}_{||}) - \hat{\Sigma}_L(Z, \mathbf{k}_{||}) - \hat{\Sigma}_R(Z, \mathbf{k}_{||})]^{-1}.\quad (5)$$

98 Note that Eq. (5) is equivalent to Dyson's equation in the standard form²⁰ of

$$\hat{G}_T(Z, \mathbf{k}_{||}) = \hat{\mathcal{G}}_T(Z, \mathbf{k}_{||}) + \hat{\mathcal{G}}_T(Z, \mathbf{k}_{||}) [\hat{\Sigma}_L(Z, \mathbf{k}_{||}) + \hat{\Sigma}_R(Z, \mathbf{k}_{||})] \hat{G}_T(Z, \mathbf{k}_{||}).\quad (6)$$

99 Here, $\hat{\Sigma}_L(Z, \mathbf{k}_{||})$ and $\hat{\Sigma}_R(Z, \mathbf{k}_{||})$ are the self-energy terms of the left and right electrodes
 100 defined by

$$\begin{aligned}\hat{\Sigma}_L(Z, \mathbf{k}_{||}) &= \hat{B}_{LT}^\dagger \hat{\mathcal{G}}_L(Z, \mathbf{k}_{||}) \hat{B}_{LT} \\ \hat{\Sigma}_R(Z, \mathbf{k}_{||}) &= \hat{B}_{TR} \hat{\mathcal{G}}_R(Z, \mathbf{k}_{||}) \hat{B}_{TR}^\dagger,\end{aligned}\quad (7)$$

101 where

$$\begin{aligned}\hat{\mathcal{G}}_L(Z, \mathbf{k}_{||}) &= [Z - \hat{H}_L(\mathbf{k}_{||})]^{-1} \\ \hat{\mathcal{G}}_R(Z, \mathbf{k}_{||}) &= [Z - \hat{H}_R(\mathbf{k}_{||})]^{-1}\end{aligned}\quad (8)$$

102 are Green's functions of the semi-infinite left and right electrodes with right- and left-side
 103 truncations, respectively. In addition, $\hat{\mathcal{G}}_T(Z, \mathbf{k}_{\parallel})$ is the Green's function associated with the
 104 isolated transition-region Hamiltonian $\hat{H}_T(\mathbf{k}_{\parallel})$:

$$\hat{\mathcal{G}}_T(Z, \mathbf{k}_{\parallel}) = \left[Z - \hat{H}_T(\mathbf{k}_{\parallel}) \right]^{-1}. \quad (9)$$

105 We used the script capital letter $\hat{\mathcal{G}}$ for describing Green's function of a semi-infinite sys-
 106 tem with one-side truncation as well as an isolated (two-side truncated) system to prevent
 107 confusing $[Z - \hat{H}_A]^{-1}$ with \hat{G}_A defined by Eq. (2), where $A = L, T$ and R . From Eqs. (5)
 108 and (6), one sees that $\hat{\mathcal{G}}_T(Z, \mathbf{k}_{\parallel})$ is extended to $\hat{G}_T(Z, \mathbf{k}_{\parallel})$ so as to include the effects of
 109 semi-infinite electrodes through the self-energy terms $\hat{\Sigma}_{\{L,R\}}(Z, \mathbf{k}_{\parallel})$.

110 B. Evaluation of self-energy terms

111 This subsection is devoted to the evaluation of the surface Green's functions of the left-
 112 and right-electrode regions $\hat{\mathcal{G}}_{\{L,R\}}(Z, \mathbf{k}_{\parallel})$ and the self-energy terms $\hat{\Sigma}_{\{L,R\}}(Z, \mathbf{k}_{\parallel})$. Hereafter,
 113 we omit the branch of the lateral Bloch vector \mathbf{k}_{\parallel} for simplicity. To set up the Hamiltonian of
 114 the electrodes, the Kohn-Sham effective potential is obtained using the unit cell consisting of
 115 $N_x \times N_y \times N_z$ grid points under the periodic boundary condition [see Fig. 3]. The Green's-
 116 function matrices for electrodes are computed using the recursive technique proposed by
 117 López Sancho *et al.*²¹ or Guinea *et al.*²² Alternatively, the matrices are evaluated by solving
 118 a quadratic eigenvalue problem.²³ In both schemes, the peculiar characteristic that the
 119 $N_x \times N_y \times N_z$ -dimensional matrices of the Hamiltonian of the electrodes are the same for
 120 each unit cell of the electrodes is employed, which implies that the dimension of the matrices
 121 for Green's functions and the self-energy terms becomes $N_x \times N_y \times N_z$. When the number of
 122 grid points increases, the computation of these matrices is demanding. In the RSFD NEGF
 123 scheme, since \hat{B}_{LT} (\hat{B}_{TR}) has only one nonzero $N(= N_x \times N_y \times N_f)$ -dimensional block-
 124 matrix element $B(\zeta_{-1})$ ($B(\zeta_{m+1})$) [see Eq. (1) and Fig. 2], the self-energy terms, which are
 125 calculated by Eq. (7), are found to take the very simple form of

$$\hat{\Sigma}_L(Z) = \begin{bmatrix} \sum_L(\zeta_0; Z) & 0 & \cdots & 0 \\ 0 & 0 & \cdots & 0 \\ \vdots & & & \vdots \\ 0 & 0 & \cdots & 0 \end{bmatrix}$$

$$\hat{\Sigma}_R(Z) = \begin{bmatrix} 0 & \cdots & 0 & 0 \\ \vdots & & & \vdots \\ 0 & \cdots & 0 & 0 \\ 0 & \cdots & 0 & \sum_R(\zeta_{m+1}; Z) \end{bmatrix}, \quad (10)$$

126 where

$$\sum_L(\zeta_0; Z) = B(\zeta_{-1})^\dagger \mathcal{G}_L(\zeta_{-1}, \zeta_{-1}; Z) B(\zeta_{-1})$$

$$\sum_R(\zeta_{m+1}; Z) = B(\zeta_{m+1}) \mathcal{G}_R(\zeta_{m+2}, \zeta_{m+2}; Z) B(\zeta_{m+1})^\dagger \quad (11)$$

127 with $\mathcal{G}_{\{L,R\}}(\zeta_k, \zeta_l; Z)$ being the N -dimensional (k, l) block-matrix element of $\hat{\mathcal{G}}_{\{L,R\}}(Z)$. In
128 practical calculations, \mathcal{N}_f is much smaller than N_z .

129 To obtain Green's function of the whole system $\hat{G}(Z)$, it is sufficient to calculate N -
130 dimensional matrices for the self-energy terms. However, although the Hamiltonians of the
131 M th and $M + 1$ th unit cell are identical, the sliced matrices of the Hamiltonian of the
132 electrodes, $H(\zeta_l^M)$ and $H(\zeta_{l+1}^M)$, are not the same, where $H(\zeta_l^M)$ is the l th N -dimensional
133 diagonal block-matrix element of the $N_x \times N_y \times N_z$ -dimensional Hamiltonian matrices of the
134 electrodes. Thus, we cannot use the two procedures above mentioned.²¹⁻²³ We introduce a
135 computational procedure for obtaining N -dimensional matrices of the surface Green's func-
136 tions and self-energy terms using ratio matrices in the OBM method,¹⁴ which are computed
137 by solving the generalized eigenvalue problem for the periodic bulk model shown in Fig. 3.

$$\Pi_1(Z) \begin{bmatrix} \Phi_n(\zeta_m^{M-1}, Z) \\ \Phi_n(\zeta_1^{M+1}, Z) \end{bmatrix} = \lambda_n(Z) \Pi_2(Z) \begin{bmatrix} \Phi_n(\zeta_m^{M-1}, Z) \\ \Phi_n(\zeta_1^{M+1}, Z) \end{bmatrix}, \quad (12)$$

138 where

$$\Pi_1(Z) = \begin{bmatrix} \Theta(\zeta_m^M, \zeta_1^M; Z) B(\zeta_m^M)^\dagger & \Theta(\zeta_m^M, \zeta_m^M; Z) B(\zeta_m^M) \\ 0 & I \end{bmatrix}$$

$$\Pi_2(Z) = \begin{bmatrix} I & 0 \\ \Theta(\zeta_1^M, \zeta_1^M; Z) B(\zeta_1^M)^\dagger & \Theta(\zeta_1^M, \zeta_m^M; Z) B(\zeta_m^M) \end{bmatrix}, \quad (13)$$

139 and $\Theta(\zeta_k^M, \zeta_l^M; Z)$ is the N -dimensional (k, l) block-matrix element of Green's function of
 140 the truncated part of the periodic Hamiltonian in the M th unit cell. In addition, Eq. (12) is
 141 the analytically continued equation of Eq. (19) in Ref. 14. Note that the generalized eigen-
 142 problem of Eq. (12) suffers numerical error owing to the extremely large and small absolute
 143 values of $\lambda(Z)$ in some cases, which prevent us from conducting an accurate computation of
 144 the eigenstates $\{\Phi_n\}$. To avoid this numerical difficulty, we introduce the following ratios of
 145 the generalized eigenstates, which are proposed in Ref. 14:

$$\begin{aligned} R^p(\zeta_0; Z) &= Q^p(\zeta_{-1}; Z)Q^p(\zeta_0; Z)^{-1} \\ R^q(\zeta_{m+2}; Z) &= Q^q(\zeta_{m+2}; Z)Q^q(\zeta_{m+1}; Z)^{-1}, \end{aligned} \quad (14)$$

146 where

$$\begin{aligned} Q^p(\zeta_l; Z) &= [\Phi_1^p(\zeta_l; Z), \Phi_2^p(\zeta_l; Z), \dots, \Phi_N^p(\zeta_l; Z)], \\ Q^q(\zeta_l; Z) &= [\Phi_1^q(\zeta_l; Z), \Phi_2^q(\zeta_l; Z), \dots, \Phi_N^q(\zeta_l; Z)]. \end{aligned} \quad (15)$$

147 Since the eigenvalues $\lambda_n(Z)$'s for a nonreal Z are divided *evenly* into two groups with $|\lambda_n| > 1$
 148 and $|\lambda_n| < 1$,²⁴ we set up the N -dimensional matrix $Q^p(\zeta_l; Z)$ and $Q^q(\zeta_l; Z)$, which gathers
 149 the N eigenstates $\{\Phi_n^p(\zeta_l; Z)\}$ and $\{\Phi_n^q(\zeta_l; Z)\}$, $n = 1, 2, \dots, N$, for a nonreal Z with $|\lambda_n| > 1$
 150 and $|\lambda_n| < 1$, respectively, using the solutions of Eq. (12). Then the accuracy of ratio
 151 matrices is improved using the following continued-fraction equations in a self-consistent
 152 manner [see Eq. (25) of Ref. 14]:

$$\begin{aligned} R^p(\zeta_1^{M+1}; Z) &= \Theta(\zeta_m^M, \zeta_m^M; Z)B(\zeta_m^M) \\ &+ \Theta(\zeta_m^M, \zeta_1^M; Z)B(\zeta_m^M)^\dagger [R^p(\zeta_1^M; Z)^{-1} - \Theta(\zeta_1^M, \zeta_1^M; Z)B(\zeta_m^M)^\dagger]^{-1} \Theta(\zeta_1^M, \zeta_m^M; Z)B(\zeta_m^M) \\ R^q(\zeta_1^{M+1}; Z) &= \Theta(\zeta_1^M, \zeta_1^M; Z)B(\zeta_m^M)^\dagger \\ &+ \Theta(\zeta_1^M, \zeta_m^M; Z)B(\zeta_m^M) [R^q(\zeta_1^{M+1}; Z)^{-1} - \Theta(\zeta_m^M, \zeta_m^M; Z)B(\zeta_m^M)]^{-1} \Theta(\zeta_m^M, \zeta_1^M; Z)B(\zeta_m^M)^\dagger. \end{aligned} \quad (16)$$

153 Now, we prove the following relation that gives a definite description of the surface Green's
 154 functions (or self-energy terms) in terms of the ratio matrices of the generalized eigenstates
 155 of Eq. (12). The surface Green's functions of the left and right electrodes are explicitly
 156 expressed as

$$\begin{aligned} \mathcal{G}_L(\zeta_{-1}, \zeta_{-1}; Z) &= R^p(\zeta_0; Z)B(\zeta_{-1})^{-1} \\ \mathcal{G}_R(\zeta_{m+2}, \zeta_{m+2}; Z) &= R^q(\zeta_{m+2}; Z)B(\zeta_{m+1})^{\dagger-1}, \end{aligned} \quad (17)$$

157 and the self-energy terms Eq. (11) are given by

$$\begin{aligned}\sum_L(\zeta_0; Z) &= B(\zeta_{-1})^\dagger R^p(\zeta_0; Z) \\ \sum_R(\zeta_{m+1}; Z) &= B(\zeta_{m+1}) R^q(\zeta_{m+2}; Z).\end{aligned}\quad (18)$$

158 Hereafter, we concentrate on proving the surface Green's functions and self-energy terms
159 of the left electrode because those of the right electrode can be derived in a similar manner.
160 The proof is derived using the results reported by Lee and Joannopoulos:²⁴ Green's function
161 $\mathcal{G}_{\{L,R\}}(\zeta_l, \zeta_m; Z \neq \text{real})$ of a crystalline bulk is a decaying function (i.e., $\mathcal{G}_{\{L,R\}} \rightarrow 0$) as
162 $|l| \rightarrow \infty$ with m fixed (or as $|m| \rightarrow \infty$ with l fixed). The eigenstates are N -independent
163 functions with respect to ζ_l with a decreasing or increasing property such that

$$\Phi_n^p(\zeta_{l-sL}; Z) = (\lambda_n)^{-s} \Phi_n^p(\zeta_l; Z) \quad (19)$$

164 Here, s is an arbitrary positive integer and L is an integer associated with the length of
165 periodicity in the z -direction. For example, $L = N_z/\mathcal{N}_f$ when N_z is a multiple of \mathcal{N}_f .
166 Furthermore, $\{\Phi_n(\zeta_l; Z)\}$ satisfies

$$-B_{l-2}^\dagger \Phi_n^p(\zeta_{l-2}; Z) + A_{l-1} \Phi_n^p(\zeta_{l-1}; Z) - B_{l-1} \Phi_n^p(\zeta_l; Z) = 0, \quad (20)$$

167 where

$$A_l = Z - H(\zeta_l) \quad \text{and} \quad B_l = B(\zeta_l). \quad (21)$$

168 Note that Eq. (20) is the Kohn-Sham equation when a complex number Z is replaced with
169 a real number E .

170 In the left electrode, the surface Green's function $\mathcal{G}_L(\zeta_l, \zeta_{-1}; Z)$ is expressed in terms of
171 $Q^p(\zeta_l; Z)$:

$$\mathcal{G}_L(\zeta_l, \zeta_{-1}; Z) = Q^p(\zeta_l; Z) Q^p(\zeta_0; Z)^{-1} (B_{-1})^{-1} \quad (l = -1, -2, \dots). \quad (22)$$

172 In the following, the derivation of Eq. (22) is demonstrated. It is straightforward from the
173 definition that $\{\mathcal{G}_L(\zeta_l, \zeta_{-1}; Z)\}$ satisfies

$$\begin{bmatrix} \ddots & \ddots & \ddots & \ddots & & & 0 \\ & -B_{-5}^\dagger & A_{-4} & -B_{-4} & & & \\ & & -B_{-4}^\dagger & A_{-3} & -B_{-3} & & \\ & & & -B_{-3}^\dagger & A_{-2} & -B_{-2} & \\ 0 & & & & -B_{-2}^\dagger & A_{-1} & \end{bmatrix} \begin{bmatrix} \vdots \\ \mathcal{G}_{-4,-1} \\ \mathcal{G}_{-3,-1} \\ \mathcal{G}_{-2,-1} \\ \mathcal{G}_{-1,-1} \end{bmatrix} = \begin{bmatrix} \vdots \\ 0 \\ 0 \\ 0 \\ I \end{bmatrix}, \quad (23)$$

174 that is,

$$\begin{aligned}
& \vdots \\
& -B_{-5}^\dagger \mathcal{G}_{-5,-1} + A_{-3} \mathcal{G}_{-4,-1} - B_{-4} \mathcal{G}_{-3,-1} = 0 \\
& -B_{-4}^\dagger \mathcal{G}_{-4,-1} + A_{-3} \mathcal{G}_{-3,-1} - B_{-3} \mathcal{G}_{-2,-1} = 0 \\
& -B_{-3}^\dagger \mathcal{G}_{-3,-1} + A_{-2} \mathcal{G}_{-2,-1} - B_{-2} \mathcal{G}_{-1,-1} = 0
\end{aligned} \tag{24}$$

175 and

$$-B_{-2}^\dagger \mathcal{G}_{-2,-1} + A_{-1} \mathcal{G}_{-1,-1} = I, \tag{25}$$

176 where

$$\mathcal{G}_{l,-1} = \mathcal{G}_L(\zeta_l, \zeta_{-1}; Z). \tag{26}$$

177 From the facts that the N -dimensional $\mathcal{G}_L(\zeta_l, \zeta_{-1}; Z \neq \text{real})$ decays deep inside the left
178 electrode ($l \rightarrow -\infty$),²⁴ we see that $\{\Phi_n^p(\zeta_l; Z)\}$ exhibits a linear independence of the decaying
179 sequences, where $n = 1, 2, \dots, N$, and Eq. (24) are the same sets of simultaneous linear
180 equations as Eq. (20) for $l \leq -1$. Therefore, \mathcal{G}_L is expanded in terms of $\{\Phi_n^p\}$ and expressed
181 as

$$\begin{aligned}
\mathcal{G}_L(\zeta_l, \zeta_{-1}; Z) &= \left[\sum_{n=1}^N f_{n1} \Phi_n^p(\zeta_l; Z), \sum_{n=1}^N f_{n2} \Phi_n^p(\zeta_l; Z), \dots, \sum_{n=1}^N f_{nN} \Phi_n^p(\zeta_l; Z) \right] \\
&= Q^p(\zeta_l; Z) F \quad (l = -1, -2, \dots),
\end{aligned} \tag{27}$$

182 where $\{f_{nn'}\}$ is a set of unknown expansion coefficients forming an N -dimensional matrix F .
183 For simplicity, the dependence of $f_{nn'}$ and F on Z and $\mathbf{k}_{||}$ is ignored. By inserting Eq. (27)
184 for $l = -1$ and -2 into Eq. (25) and subsequently using Eq. (20) for $l = 0$, we obtain

$$F = Q^p(\zeta_0; Z)^{-1} (B_{-1})^{-1}. \tag{28}$$

185 By substituting Eq. (28) into Eq. (27), Eq. (22) is obtained.

186 Next, we carry out the limiting procedure in Eq. (22) to obtain the *retarded* Green's
187 function. Since the pairing characteristic of $\lambda(E)$'s implies that there are always equal
188 numbers of reflected waves Φ_n^{ref} and transmitted waves Φ_n^{tra} for a given energy E and lateral
189 Bloch wave vector $\mathbf{k}_{||}$, we obtain

$$\begin{aligned}
\lim_{\eta \rightarrow 0^+} \Phi_n^p(\zeta_l; E + i\eta) &= \Phi_n^{ref}(\zeta_l; E), \\
\lim_{\eta \rightarrow 0^+} Q^p(\zeta_l; E + i\eta) &= Q^{ref}(\zeta_l; E), \\
\lim_{\eta \rightarrow 0^+} R^p(\zeta_l; E + i\eta) &= R^{ref}(\zeta_l; E),
\end{aligned} \tag{29}$$

190 where $Q^{ref}(\zeta_l; E)$ is an N -dimensional matrix that gathers left-propagating Bloch waves
 191 ($|\lambda(E)| = 1$ and $\text{Re}(\lambda(E)) < 0$) and rightward increasing evanescent waves ($|\lambda(E)| > 1$):

$$Q^{ref}(\zeta_l; E) = \left[\Phi_1^{ref}(\zeta_l; E), \Phi_2^{ref}(\zeta_l; E), \dots, \Phi_N^{ref}(\zeta_l; E) \right], \quad (30)$$

192 and

$$R^{ref}(\zeta_l; E) = Q^{ref}(\zeta_{l-1}; E)Q^{ref}(\zeta_l; E)^{-1}. \quad (31)$$

193 Note that the eigestates with $|\lambda(Z)| = 1$ are absent when $\eta \neq 0$,²⁴ while those with $|\lambda(Z)| = 1$
 194 exist in the case of real-number energy.¹⁴

195 Finally, the retarded Green's function is

$$\begin{aligned} \mathcal{G}_L^r(\zeta_{-1}, \zeta_{-1}; E) &= \lim_{\eta \rightarrow 0^+} \mathcal{G}_L(\zeta_{-1}, \zeta_{-1}; E + i\eta) \\ &= Q^{ref}(\zeta_{-1}; E)Q^{ref}(\zeta_0; E)^{-1}(B_{-1})^{-1} \\ &= R^{ref}(\zeta_0; Z)B(\zeta_{-1})^{-1}, \end{aligned} \quad (32)$$

196 and hence the retarded self-energy term is

$$\hat{\Sigma}_{\{L,R\}}^r(E) = \lim_{\eta \rightarrow 0^+} \hat{\Sigma}_{\{L,R\}}(E + i\eta). \quad (33)$$

197 Several researchers have investigated the representation of the surface Green's functions
 198 by generalized eigenstates.^{3,4,24} Note that the above relations are particularly attractive be-
 199 cause they allow us to directly evaluate the retarded surface Green's functions and retarded
 200 self-energy terms at a purely real E without using the finite broadening (or smearing) param-
 201 eter η . More interestingly, we can reduce the dimension of the matrices of Green's functions
 202 and the self-energy terms from $N_x \times N_y \times N_z$ to N while keeping mathematical rigorousness.

203 C. Evaluation of whole Green's function in the transition region

204 Green's function of the whole system portioned to the transition region, $\hat{G}_T(Z)$, is given by
 205 Eq. (5). In this subsection, we present the analytic expression of Eq. (5), which is equivalent
 206 to the exact solution of Dyson's equation Eq. (6). In the general case of the Hamiltonian
 207 matrix \hat{H}_T being not necessarily sparse, the simplest way to calculate $\hat{G}_T(Z)$ of Eq. (5)
 208 might be to carry out direct matrix inversion. In practice, however, it is computationally
 209 difficult to perform inversion calculations with large matrices. In what follows, we show that

210 there exists an efficient approach to computing the non-Hermit $\hat{G}_T(E)$ on the basis of the
 211 OBM scheme.

212 Let us consider the l th column of $\hat{G}_T(Z)$, i.e., $[G_T(\zeta_0, \zeta_l; Z), G_T(\zeta_1, \zeta_l; Z), \dots, G_T(\zeta_{m+1}, \zeta_l; Z)]^t$
 213 ($l = 0, 1, 2, \dots, m + 1$). From Eq. (5), one sees that the l th column satisfies

$$\left[Z - \hat{H}_T - \hat{\Sigma}_L(Z) - \hat{\Sigma}_R(Z) \right] \begin{bmatrix} G_T(\zeta_0, \zeta_l; Z) \\ G_T(\zeta_1, \zeta_l; Z) \\ \vdots \\ G_T(\zeta_l, \zeta_l; Z) \\ \vdots \\ G_T(\zeta_m, \zeta_l; Z) \\ G_T(\zeta_{m+1}, \zeta_l; Z) \end{bmatrix} = \begin{bmatrix} 0 \\ 0 \\ \vdots \\ 0 \\ I \\ 0 \\ \vdots \\ 0 \\ 0 \end{bmatrix} \leftarrow \text{the } l\text{th} \quad (34)$$

214 by virtue of a simple form of the self-energy matrices, Eq. (10). Using Green's function of
 215 the truncated part of the Hamiltonian $\hat{\mathcal{G}}_T(Z)$ defined in Eq. (9), the whole Green's function
 216 in the transition region is given by

$$\begin{bmatrix} G_T(\zeta_0, \zeta_l; Z) \\ G_T(\zeta_1, \zeta_l; Z) \\ \vdots \\ G_T(\zeta_l, \zeta_l; Z) \\ \vdots \\ G_T(\zeta_m, \zeta_l; Z) \\ G_T(\zeta_{m+1}, \zeta_l; Z) \end{bmatrix} = \hat{\mathcal{G}}_T(Z) \begin{bmatrix} \sum_L(\zeta_0; Z)G_T(\zeta_0, \zeta_l; Z) \\ 0 \\ \vdots \\ 0 \\ I \\ 0 \\ \vdots \\ 0 \\ \sum_R(\zeta_{m+1}; Z)G_T(\zeta_{m+1}, \zeta_l; Z) \end{bmatrix} \leftarrow \text{the } l\text{th} \quad (35)$$

217 Equation (35) is a matching relation with regard to Green's function $\{G_T(\zeta_k, \zeta_l)\}$, which
 218 is an analogous one with regard to the wave function $\{\Psi(z_k)\}$ [see Eq. (1) of Ref. 14].
 219 The surface Green's-function matching theory has been pioneered by García-Moliner and
 220 Velasco.²⁵ From Eq. (34), we see that once Green's function of the truncated part of the
 221 Hamiltonian $\hat{\mathcal{G}}_T(Z) = [Z - \hat{H}_T]^{-1}$ is known, the elements of the whole Green's function

222 $G_T(\zeta_0, \zeta_l; Z)$ and $G_T(\zeta_{m+1}, \zeta_l; Z)$ are calculated using

$$\begin{aligned}
& \begin{bmatrix} \mathcal{G}_T(\zeta_0, \zeta_0; Z) \sum_L(\zeta_0; Z) - I & \mathcal{G}_T(\zeta_0, \zeta_{m+1}; Z) \sum_R(\zeta_{m+1}; Z) \\ \mathcal{G}_T(\zeta_{m+1}, \zeta_0; Z) \sum_L(\zeta_0; Z) & \mathcal{G}_T(\zeta_{m+1}, \zeta_{m+1}; Z) \sum_R(\zeta_{m+1}; Z) - I \end{bmatrix} \\
& \quad \times \begin{bmatrix} G_T(\zeta_0, \zeta_l; Z) \\ G_T(\zeta_{m+1}, \zeta_l; Z) \end{bmatrix} = - \begin{bmatrix} \mathcal{G}_T(\zeta_0, \zeta_l; Z) \\ \mathcal{G}_T(\zeta_{m+1}, \zeta_l; Z) \end{bmatrix}. \quad (36)
\end{aligned}$$

223 Here, $\mathcal{G}_T(\zeta_k, \zeta_l; Z)$ is the N -dimensional (k, l) block-matrix element of $\hat{\mathcal{G}}_T(Z)$. Equation (36),
224 which is a $2N$ simultaneous linear equation with respect to $G_T(\zeta_0, \zeta_l; Z)$ and $G_T(\zeta_{m+1}, \zeta_l; Z)$,
225 manifests boundary-value (surface) matching for Green's function of the whole system. To
226 calculate the electronic structure in the transition region, the diagonal elements of the
227 Green's-function matrix, $G_T(\zeta_l, \zeta_l; Z)$, are required. On the other hand, when we are only
228 interested in the transport property, it is sufficient to compute Green's functions on the
229 matching planes, $G_T^r(\zeta_0, \zeta_0; E)$, $G_T^r(\zeta_{m+1}, \zeta_0; E)$, $G_T^r(\zeta_0, \zeta_{m+1}; E)$, and $G_T^r(\zeta_{m+1}, \zeta_{m+1}; E)$. In
230 the following, we show the analytic expressions for the solution of Eq. (36) in the cases of
231 $l = 0$ and $l = m + 1$, which are required in the calculation of the conductance in the NEGF
232 formalism.

233 For $l = 0$ and $l = m + 1$,

$$\begin{aligned}
G_T(\zeta_0, \zeta_0; Z) &= \tilde{\mathcal{G}}_T(\zeta_0, \zeta_0; Z) \left[I - \sum_L(\zeta_0; Z) \tilde{\mathcal{G}}_T(\zeta_0, \zeta_0; Z) \right]^{-1}, \\
G_T(\zeta_{m+1}, \zeta_0; Z) &= \left[I - \mathcal{G}_T(\zeta_{m+1}, \zeta_{m+1}; Z) \sum_R(\zeta_{m+1}; Z) \right]^{-1} \\
&\quad \times \mathcal{G}_T(\zeta_{m+1}, \zeta_0; Z) \left[I - \sum_L(\zeta_0; Z) \tilde{\mathcal{G}}_T(\zeta_0, \zeta_0; Z) \right]^{-1}, \\
G_T(\zeta_0, \zeta_{m+1}; Z) &= \left[I - \mathcal{G}_T(\zeta_0, \zeta_0; Z) \sum_L(\zeta_0; Z) \right]^{-1} \mathcal{G}_T(\zeta_0, \zeta_{m+1}; Z) \\
&\quad \times \left[I - \sum_R(\zeta_{m+1}; Z) \tilde{\mathcal{G}}_T(\zeta_{m+1}, \zeta_{m+1}; Z) \right]^{-1}, \\
G_T(\zeta_{m+1}, \zeta_{m+1}; Z) &= \tilde{\mathcal{G}}_T(\zeta_{m+1}, \zeta_{m+1}; Z) \left[I - \sum_R(\zeta_{m+1}; Z) \tilde{\mathcal{G}}_T(\zeta_{m+1}, \zeta_{m+1}; Z) \right]^{-1}, \quad (37)
\end{aligned}$$

234 where $\tilde{\mathcal{G}}_T$ is a modified \mathcal{G}_T under the influence of the self-energy term $\sum_{\{L,R\}}$, which is

235 expressed as

$$\begin{aligned}
\tilde{\mathcal{G}}_T(\zeta_0, \zeta_0; Z) &= \mathcal{G}_T(\zeta_0, \zeta_0; Z) \\
&+ \mathcal{G}_T(\zeta_0, \zeta_{m+1}; Z) \Sigma_R(\zeta_{m+1}; Z) \\
&\times \left[I - \mathcal{G}_T(\zeta_{m+1}, \zeta_{m+1}; Z) \Sigma_R(\zeta_{m+1}; Z) \right]^{-1} \mathcal{G}_T(\zeta_{m+1}, \zeta_0; Z), \\
\tilde{\mathcal{G}}_T(\zeta_{m+1}, \zeta_{m+1}; Z) &= \mathcal{G}_T(\zeta_{m+1}, \zeta_{m+1}; Z) \\
&+ \mathcal{G}_T(\zeta_{m+1}, \zeta_0; Z) \Sigma_L(\zeta_0; Z) \\
&\times \left[I - \mathcal{G}_T(\zeta_0, \zeta_0; Z) \Sigma_L(\zeta_0; Z) \right]^{-1} \mathcal{G}_T(\zeta_0, \zeta_{m+1}; Z). \tag{38}
\end{aligned}$$

236 It is easy to ensure that the G_T 's given by Eqs. (37) – (38) satisfy Eq. (36), and therefore,
237 they are the exact analytic solutions of Eq. (5) as well as Dyson's equation of Eq. (6).
238 Finally, a retarded Green's function is obtainable by carrying out the limiting procedure:

$$G_T^r(\zeta_k, \zeta_l; E) = \lim_{\eta \rightarrow 0^+} G_T(\zeta_k, \zeta_l; E + i\eta). \tag{39}$$

239 Note that the block matrices of Green's function, $G_T^r(\zeta_0, \zeta_0; E)$, $G_T^r(\zeta_{m+1}, \zeta_0; E)$, $G_T^r(\zeta_0, \zeta_{m+1}; E)$,
240 and $G_T^r(\zeta_{m+1}, \zeta_{m+1}; E)$, are not $N_x \times N_y \times N_z$ -dimensional, but N -dimensional because the
241 matrices of the self-energy terms have already been reduced to N -dimensional in the pre-
242 ceding subsection.

243 D. Description of scattering wave function in terms of whole Green's function

244 We next show that the relationship between the retarded Green's functions and the
245 scattering wave functions is expressed as

$$\Psi_j(\zeta_l; E) = iG_T^r(\zeta_l, \zeta_0; E) \Gamma_L(\zeta_0; E) \Phi_j^{in}(\zeta_0; E) \quad (0 \leq l \leq m+1), \tag{40}$$

246 where $\Gamma_L(\zeta_l; E)$ is the coupling matrix, which describes the 'coupling strength' of the tran-
247 sition region to the left electrode at ζ_0 , and is defined by

$$\Gamma_L(\zeta_0; E) = i \left[\Sigma_L^r(\zeta_0; E) - \Sigma_L^a(\zeta_0; E) \right] \quad (\Sigma_L^a(\zeta_0; E) = \Sigma_L^r(\zeta_0; E)^\dagger). \tag{41}$$

248 From Eq. (6) of Ref. 26, the scattering wave function incoming from deep inside the left

249 electrode is expressed as

$$\begin{aligned}
& \left[E - \hat{H}_T - \hat{\Sigma}_L^r(E) - \hat{\Sigma}_R^r(E) \right] \begin{bmatrix} \Psi_j(\zeta_0; E) \\ \Psi_j(\zeta_1; E) \\ \vdots \\ \Psi_j(\zeta_m; E) \\ \Psi_j(\zeta_{m+1}; E) \end{bmatrix} \\
&= \begin{bmatrix} B(\zeta_{-1})^\dagger \Phi_j^{in}(\zeta_{-1}; E) - \sum_L^r(\zeta_0; E) \Phi_j^{in}(\zeta_0; E) \\ 0 \\ \vdots \\ 0 \\ 0 \end{bmatrix}. \tag{42}
\end{aligned}$$

250 The incident wave from the right electrode can be derived in a similar manner. By the
251 definition of the retarded Green's function of the whole system in Eq. (5), Eq. (42) is
252 rewritten as

$$\begin{bmatrix} \Psi_j(\zeta_0; E) \\ \Psi_j(\zeta_1; E) \\ \vdots \\ \Psi_j(\zeta_m; E) \\ \Psi_j(\zeta_{m+1}; E) \end{bmatrix} = \hat{G}_T^r(E) \begin{bmatrix} B(\zeta_{-1})^\dagger \Phi_j^{in}(\zeta_{-1}; E) - \sum_L^r(\zeta_0; E) \Phi_j^{in}(\zeta_0; E) \\ 0 \\ \vdots \\ 0 \\ 0 \end{bmatrix}. \tag{43}$$

253 Now the ratio matrix R^{in} in the left electrode ($l \leq 0$) is introduced along a similar line
254 into the definition of R^{ref} :

$$R^{in}(\zeta_l; E) = Q^{in}(\zeta_{l-1}; E) Q^{in}(\zeta_l; E)^{-1}, \tag{44}$$

255 where

$$Q^{in}(\zeta_l; E) = \left[\Phi_1^{in}(\zeta_l; E), \Phi_2^{in}(\zeta_l; E), \dots, \Phi_N^{in}(\zeta_l; E) \right], \tag{45}$$

256 which is assumed to include not only ordinary right-propagating incident Bloch waves but
257 also leftward-decreasing evanescent waves. From the definition of $R^{in}(\zeta_0; E)$, it is straight-
258 forward to state that

$$\Phi_j^{in}(\zeta_{-1}; E) = R^{in}(\zeta_0; E) \Phi_j^{in}(\zeta_0; E). \tag{46}$$

259 Furthermore, the relationship between the retarded self-energy term $\sum_L^r(\zeta_0; E)^\dagger$ and $R^{in}(\zeta_0; E)$
 260 is expressed as

$$\sum_L^r(\zeta_0; E)^\dagger = B(\zeta_{-1})^\dagger R^{in}(\zeta_0; E) \quad (47)$$

261 similarly to that of $\sum_L^r(\zeta_0; E)$ and $R^{ref}(\zeta_0; E)$ in subsection II B. From Eqs. (43), (46) and
 262 (47), the scattering wave function $\Psi_j(\zeta_l; E)$ for $0 \leq l \leq m + 1$ can be written as

$$\begin{aligned} \Psi_j(\zeta_l; E) &= G_T^r(\zeta_l, \zeta_0; E) \left[B(\zeta_{-1})^\dagger \Phi_j^{in}(\zeta_{-1}; E) - \sum_L^r(\zeta_0; E) \Phi_j^{in}(\zeta_0; E) \right] \\ &= -G_T^r(\zeta_l, \zeta_0; E) \left[\sum_L^r(\zeta_0; E) - \sum_L^r(\zeta_0; E)^\dagger \right] \Phi_j^{in}(\zeta_0; E) \\ &= iG_T^r(\zeta_l, \zeta_0; E) \Gamma_L(\zeta_0; E) \Phi_j^{in}(\zeta_0; E). \end{aligned} \quad (48)$$

263 The derivation of Eq. (40) in a different manner is given in Ref. 8, and the expression using
 264 $N_x \times N_y \times N_z$ -dimensional matrices is also introduced in Ref. 27.

265 E. Conductance

266 We finally address the problem of electronic transport within the framework of the RSFD
 267 Green's-function approach. Here, we consider the case of the incident wave Φ_j^{in} incoming
 268 from deep inside the left electrode. We can prove that the Landauer-Büttiker formula²⁸
 269 $G = 2e^2/h \sum_{i,j} |t_{ij}|^2 v'_i/v_j$ describing the conductance G has the expression in terms of
 270 Green's functions $G_T^{\{r,a\}}$ and the self-energy matrices $\sum_{\{L,R\}}^{\{r,a\}}$, where e is the electron charge,
 271 h is Planck's constant, t_{ij} is the transmission coefficient for the j th incident wave to the
 272 i th outgoing wave, and $v_j(v'_i)$ is the group velocity of the state $\Phi_j^{in}(\zeta_0; E)(\Phi_i^{tra}(\zeta_{m+1}; E))$
 273 through the x - y plane at $\zeta_0(\zeta_{m+1})$. In the OBM scheme, group velocity is expressed as

$$\begin{aligned} v_j &= L_z \left[\Phi_j^{in}(\zeta_0; E)^\dagger \Gamma_L(\zeta_0; E) \Phi_j^{in}(\zeta_0; E) \right] \\ v'_i &= L_z \left[\Phi_i^{tra}(\zeta_{m+1}; E)^\dagger \Gamma_R(\zeta_{m+1}; E) \Phi_i^{tra}(\zeta_{m+1}; E) \right] \end{aligned} \quad (49)$$

274 where L_z is the length of the unit cell in the z -direction. The proof of Eq. (49) is given in
 275 Appendix A.

276 The scattering wave function $\Psi_j(\zeta_l; E)$ corresponding to the j th incident wave $\Phi_j^{in}(\zeta_0; E)$
 277 is given by a linear combination of transmitted waves $\Phi_i^{tra}(\zeta_l; E)$ inside the right electrode
 278 ($l \geq m + 1$) with a transmission coefficient t_{ij} , i.e.,

$$\Psi_j(\zeta_l; E) = \sum_{i=1}^N t_{ij} \Phi_i^{tra}(\zeta_l; E) = Q^{tra}(\zeta_l; E) [t_{1j}, t_{2j}, \dots, t_{Nj}]^t, \quad (50)$$

279 where $Q^{tra}(\zeta_l; E)$ is an N -dimensional matrix that gathers right-propagating Bloch waves
 280 ($|\lambda(E)| = 1$ and $\text{Re}(\lambda(E)) > 0$) and rightward-decreasing evanescent waves ($|\lambda(E)| < 1$) of
 281 $\Phi_i^{tra}(\zeta_l; E)$, i.e.,

$$Q^{tra}(\zeta_l; E) = \left[\Phi_1^{tra}(\zeta_l; E), \Phi_2^{tra}(\zeta_l; E), \dots, \Phi_N^{tra}(\zeta_l; E) \right]. \quad (51)$$

282 From Eqs. (40) and (50) for $l = m + 1$, we have

$$[t_{1j}, t_{2j}, \dots, t_{Nj}]^t = iQ^{tra}(\zeta_{m+1}; E)^{-1} G_T^r(\zeta_{m+1}, \zeta_0; E) \Gamma_L(\zeta_0; E) \Phi_{L,j}^{in}(\zeta_0; E) \quad (52)$$

283 and then obtain

$$T = iQ^{tra}(\zeta_{m+1}; E)^{-1} G_T^r(\zeta_{m+1}, \zeta_0; E) \Gamma_L(\zeta_0; E) Q^{in}(\zeta_0; E). \quad (53)$$

284 Here, T is the transmission-coefficient matrix

$$T = \begin{bmatrix} t_{11} & t_{12} & \cdots & t_{1N} \\ t_{21} & t_{22} & \cdots & t_{2N} \\ & & \cdots & \\ t_{N1} & t_{N2} & \cdots & t_{NN} \end{bmatrix} \quad (54)$$

285 and $Q^{in}(\zeta_0; E)$ is the matrix defined by Eq. (45). Note that the expression

$$\sum_{i,j} |t_{ij}|^2 \frac{v'_i}{v_j} = \text{Tr} \left[\mathcal{V}^{-1} T^\dagger \mathcal{V}' T \right] \quad (55)$$

286 holds, with $\mathcal{V}^{(\prime)}$ being a diagonal matrix whose elements are $v_i^{(\prime)} \delta_{ij}$. By substituting Eq. (53)
 287 into the right-hand side of Eq. (55), we find

$$\begin{aligned} \sum_{i,j} |t_{ij}|^2 \frac{v'_i}{v_j} &= \text{Tr} \left[\Gamma_L(\zeta_0; E) Q^{in}(\zeta_0; E) \mathcal{V}^{-1} Q^{in}(\zeta_0; E)^\dagger \Gamma_L(\zeta_0; E) G_T^a(\zeta_0, \zeta_{m+1}; E) \right. \\ &\quad \left. \times Q^{tra}(\zeta_{m+1}; E)^\dagger \mathcal{V}' Q^{tra}(\zeta_{m+1}; E)^{-1} G_T^r(\zeta_{m+1}, \zeta_0; E) \right]. \end{aligned} \quad (56)$$

288 Here, ‘Tr’ stands for the trace, i.e., the sum of the diagonal matrix elements, and the cyclic
 289 property of the trace is used. From Eqs. (45), (49), and (51), the relations

$$\begin{aligned} \mathcal{V} &= iL_z Q^{in}(\zeta_0; E)^\dagger \Gamma_L(\zeta_0; E) Q^{in}(\zeta_0; E) \\ \mathcal{V}' &= iL_z Q^{tra}(\zeta_{m+1}; E)^\dagger \Gamma_R(\zeta_{m+1}; E) Q^{tra}(\zeta_{m+1}; E) \end{aligned} \quad (57)$$

290 are derived, and then

$$\begin{aligned}
G &= \frac{2e^2}{h} \sum_{i,j} |t_{ij}|^2 \frac{v'_i}{v_j} \\
&= \frac{2e^2}{h} \text{Tr} \left[\Gamma_L(\zeta_0; E) G_T^a(\zeta_0, \zeta_{m+1}; E) \Gamma_R(\zeta_{m+1}; E) G_T^r(\zeta_{m+1}, \zeta_0; E) \right] \\
&= \frac{2e^2}{h} \text{Tr} \left[\Gamma_L(\zeta_0; E) G_T^r(\zeta_0, \zeta_{m+1}; E) \Gamma_R(\zeta_{m+1}; E) G_T^a(\zeta_{m+1}, \zeta_0; E) \right]
\end{aligned} \tag{58}$$

291 are established. Here, the advanced Green's function is

$$G_T^a(\zeta_k, \zeta_l; E) = G_T^r(\zeta_l, \zeta_k; E)^\dagger. \tag{59}$$

292 Equation (58) is a well-known formula²⁹ in the NEGF formalism pioneered by Keldysh.¹
293 The equality of the last line in Eq. (58) is also verified with a similar consideration of the
294 case of incident waves incoming from the right electrode. One of the advantages of the
295 Green's-function approach is that the conductance is calculated without the knowledge of
296 well-defined asymptotic wave functions in the transition region.

297 **III. TRANSPORT PROPERTY OF BN RING CONNECTED TO CNT ELEC-** 298 **TRODES**

299 To demonstrate the applicability of the RSFD NEGF method and the importance of the
300 interpretation using scattering wave functions, the transport property of the C/BNNT where
301 one carbon ring of (9,0) CNT is replaced with a BN ring is examined. Figure 4 shows the
302 computational model, in which the C/BNNT is sandwiched between the CNT electrodes.
303 A valence electron-ion interaction is described using norm-conserving pseudopotentials³⁰
304 generated by the scheme proposed by Troullier and Martins.³¹ Exchange and correlation
305 effects are treated within the local density approximation¹⁵ of the density functional theory.
306 To determine the Kohn-Sham effective potential, we use a conventional supercell under a
307 periodic boundary condition in all directions with a real-space grid spacing of ~ 0.24 Å; the
308 dimensions of the supercell are $L_x = 13.34$ Å, $L_y = 13.34$ Å, and $L_z = 4.32$ Å, where L_x
309 and L_y are the lateral lengths of the supercell in the x - and y -directions perpendicular to
310 the nanotube axis, respectively, and L_z is the length in the z -direction. Then we compute
311 the scattering wave functions obtained non-self-consistently. It has been reported that this
312 procedure is just as accurate in the linear response regime but significantly more efficient than

313 performing computations self-consistently on a scattering-wave basis.³² The conductance is
314 calculated using Eq. (58).

315 Figure 5 shows the conductance spectrum of the C/BNNT. To investigate states that
316 actually contribute to electron transport, the eigenchannels are computed by diagonalizing
317 the Hermit matrix $T^\dagger T$, where T is the transmission-coefficient matrix defined in Eq. (54).¹⁰
318 For reference, we plot in Fig. 6 the band structures of the CNT and C/BNNT in the periodic
319 supercell used to obtain the Kohn-Sham effective potential. It is reported in the other DFT
320 calculations that the band gap of the (9,0) CNT opens even though the (9,0) CNT is expected
321 to be metallic by the zone folding of the tight-binding approximation;³³ the zero-conductance
322 region around the Fermi level corresponds to the fundamental band gap of the (9,0) CNT.
323 In addition, the bands of the C/BNNT indicated by β and γ doubly degenerate as well as
324 the bands of the CNT indicated by α at approximately the Fermi level. One can see in
325 Fig. 5 that two channels actually contribute to the transport in the vicinity of the Fermi
326 level and significant peaks due to the resonant tunneling through the dispersionless bands
327 indicated by γ are not observed in the conductance spectrum. Since a real-space picture of
328 the wave function helps us to understand the transport phenomenon, the spatial behaviors
329 of the C/BNNT and CNT states, which are relevant to the electron transport, are shown
330 in Fig. 7. We plot the wave functions at Γ point because the symmetry in the x - y plane
331 is insensitive with respect to the variation in k_z in a one-dimensional Brillouin zone. For
332 comparison, the behaviors of the wave functions indicated by α , β , and γ in Fig. 6 are also
333 plotted in Fig. 8. The wave function of the energetically dispersive bands of the C/BNNT
334 (indicated by β) shows threefold rotational symmetry with respect to tube axis, whereas
335 that of the dispersionless bands (indicated by γ) shows fivefold symmetry. The energetically
336 dispersive bands can contribute to electron transport because the spatial symmetry of the
337 wave functions of the bands corresponds to that of the wave functions coming from the left
338 CNT electrode and outgoing to the right CNT electrode indicated by α . In contrast, the
339 symmetry of the dispersionless bands does not agree with those of the coming and outgoing
340 waves, and thus the wave functions from the CNT electrodes are hardly connected to the
341 wave function of the dispersionless bands, resulting in a small contribution to the electron
342 transport. These results imply that the interpretation using the scattering wave function,
343 which does not explicitly appear in the NEGF method, is important for the investigation of
344 the transport properties of nanoscale systems.

345 **IV. SUMMARY**

346 We have proposed an efficient procedure for RSFD NEGF calculations for obtaining
347 the transport property of nanoscale systems. Since the number of grid points in real-space
348 methods is larger than that of basis in the tight-binding approach, the computational cost to
349 obtain the surface Green's functions and self-energy terms has been the bottleneck. Using the
350 ratio matrices in the OBM method, the present procedure greatly reduces the computational
351 cost to obtain the surface Green's functions and self-energy terms of the electrodes as well
352 as the Green's functions of the whole system without loss of mathematical rigorousness. In
353 addition, we proved that scattering wave functions, which provide us a real-space picture of
354 the scattering process, can be obtainable by the present scheme.

355 The transport property of the BN ring connected to the carbon nanotube electrode is
356 investigated using the present method. By examining the rotational symmetry of wave
357 functions at the matching plane, we found that states that are energetically dispersionless
358 in a one-dimensional Brillouin zone hardly contribute to the electron transport because of
359 the difference in the rotational symmetry of wave functions with respect to the tube axis.
360 This result indicates that the real-space picture of the scattering wave function, which is
361 not necessary to be taken into account to calculate the transport property in the NEGF
362 formalism, helps us to interpret transport phenomena in the transition region.

363 Since the OBM method is developed for the RSFD scheme, the present technique allows
364 us to efficiently obtain quantities for the NEGF method in a real-space representation. In
365 particular, the RSFD scheme of first-principles calculations is a method that has the advan-
366 tage to scale with massively parallel architectures and has this potential without compromise
367 on precision. Moreover, this scheme is free of problems concerning the completeness of the
368 basis set such as in the methods using localized basis sets of either atomic orbitals or Gaus-
369 sians. Therefore, the present procedure opens the possibility for executing large-scale RSFD
370 NEGF calculations using massively parallel computers with a high degree of accuracy.

371 **ACKNOWLEDGEMENTS**

372 This research was partially supported by Strategic Japanese-German Cooperative Pro-
373 gram from Japan Science and Technology Agency and Deutsche Forschungsgemeinschaft,

374 by the Computational Materials Science Initiative (CMSI), and by a Grant-in-Aid for Sci-
375 entific Research on Innovative Areas (Grant No. 22104007) from the Ministry of Education,
376 Culture, Sports, Science and Technology, Japan. The numerical calculation was carried out
377 using the computer facilities of the Institute for Solid State Physics at the University of
378 Tokyo and Center for Computational Sciences at University of Tsukuba.

379 **Appendix A: Group velocity**

380 For completeness, we introduce the expression for the group velocity in this appendix.

381 Group velocity is written as

$$v_g = \frac{\partial E}{\partial k(E)} \mathbf{u}^\dagger(E) \mathbf{u}(E), \quad (\text{A1})$$

382 where $k(E)$ is a Bloch wave vector with E being the Kohn-Sham energy and $\mathbf{u}(E)$ is an
 383 $N_x \times N_y \times N_z$ -dimensional columnar vector consisting of $\Phi_j(\zeta_l^M, E)$ of the M th unit cell (see
 384 Fig. 2):

$$\mathbf{u}(E) = [\Phi_j(\zeta_1^M; E), \Phi_j(\zeta_2^M; E), \dots, \Phi_j(\zeta_N^M; E)]^t. \quad (\text{A2})$$

385 The propagating wave obeys the Kohn-Sham equation

$$\hat{H}_{per}^M(k(E), \mathbf{k}_{||}) \mathbf{u}(E) = E \mathbf{u}(E), \quad (\text{A3})$$

386 where $\hat{H}_{per}^M(k(E))$ is the $N_x \times N_y \times N_z$ -dimensional *periodic* Hamiltonian of the M th unit
 387 cell,

$$= \begin{bmatrix} \hat{H}_{per}^M(k(E), \mathbf{k}_{||}) & & & & & & \\ H(\zeta_1^M; \mathbf{k}_{||}) & B(\zeta_1^M) & 0 & \dots & 0 & e^{-ik(E)L_z} B(\zeta_m^M)^\dagger & \\ B(\zeta_1^M)^\dagger & H(\zeta_2^M; \mathbf{k}_{||}) & B(\zeta_2^M) & & & 0 & \\ 0 & \ddots & \ddots & \ddots & & \vdots & \\ \vdots & & \ddots & \ddots & \ddots & 0 & \\ 0 & & B(\zeta_{m-2}^M)^\dagger & H(\zeta_{m-1}^M; \mathbf{k}_{||}) & B(\zeta_{m-1}^M) & & \\ e^{ik(E)L_z} B(\zeta_m^M) & 0 & \dots & 0 & B(\zeta_{m-1}^M)^\dagger & H(\zeta_m^M; \mathbf{k}_{||}) & \end{bmatrix}. \quad (\text{A4})$$

388 Differentiating the eigenvalue equation of Eq. (A3) with respect to $k(E)$ and multiplying
 389 $\mathbf{u}(E)^\dagger$ from the left-hand side of the resultant equation yields

$$\mathbf{u}(E)^\dagger \frac{d\hat{H}_{per}^M}{dk(E)} \mathbf{u}(E) = \frac{dE}{dk(E)} \mathbf{u}(E)^\dagger \mathbf{u}(E). \quad (\text{A5})$$

390 From Eq. (A4), one finds that

$$\frac{d\hat{H}_{per}}{dk(E)} = \begin{bmatrix} 0 & 0 \dots 0 & -iL_z e^{-ik(E)L_z} B(\zeta_m^M)^\dagger \\ 0 & 0 \dots 0 & 0 \\ \vdots & \vdots & \vdots \\ iL_z e^{ik(E)L_z} B(\zeta_m^M) & 0 \dots 0 & 0 \end{bmatrix} \quad (\text{A6})$$

391 and

$$\begin{aligned}
\mathbf{u}(E)^\dagger \frac{d\hat{H}_{per}}{dk(E)} \mathbf{u}(E) &= iL_z e^{ik(E)L_z} \Phi_j(\zeta_m^M; E)^\dagger B(\zeta_m^M) \Phi_j(\zeta_1^M; E) \\
&\quad - iL_z e^{-ik(E)L_z} \Phi_j(\zeta_1^M; E)^\dagger B(\zeta_m^M)^\dagger \Phi_j(\zeta_m^M; E) \\
&= iL_z \Phi_j(\zeta_m^M; E)^\dagger B(\zeta_m^M) \Phi_j(\zeta_1^{M+1}; E) \\
&\quad - iL_z \Phi_j(\zeta_1^{M+1}; E)^\dagger B(\zeta_m^M)^\dagger \Phi_j(\zeta_m^M; E) \\
&= iL_z \Phi_j(\zeta_m^{M-1}; E)^\dagger B(\zeta_m^M) \Phi_j(\zeta_1^M; E) \\
&\quad - iL_z \Phi_j(\zeta_1^M; E)^\dagger B(\zeta_m^M)^\dagger \Phi_j(\zeta_m^{M-1}; E). \tag{A7}
\end{aligned}$$

392 Here, the second step follows from the Bloch condition

$$\Phi_j(\zeta_1^{M+1}; E) = e^{ik(E)L_z} \Phi_j(\zeta_1^M; E), \tag{A8}$$

393 and the flux conservation is used in the last step. From Eqs. (A1), (A5) and (A7), group
394 velocity is given by

$$v_g = iL_z \left[\Phi_j(\zeta_m^{M-1}; E)^\dagger B(\zeta_m^M) \Phi_j(\zeta_1^M; E) - \Phi_j(\zeta_1^M; E)^\dagger B(\zeta_m^M)^\dagger \Phi_j(\zeta_m^{M-1}; E) \right], \tag{A9}$$

395 where the normalization of the Bloch states is defined as $\sum_l \Phi_j(\zeta_l^M; E)^\dagger \Phi_j(\zeta_l^M; E) = 1$.

396 Furthermore, making use of Eqs. (41), (46), and (47), we have a simpler expression for
397 group velocity in terms of the coupling matrix:

$$v_g = L_z \left[\Phi_j(\zeta_1^M; E)^\dagger \Gamma(\zeta_1^M; E) \Phi_j(\zeta_1^M; E) \right]. \tag{A10}$$

398 ¹ L.V. Keldysh, Zh. Eksp. Teor. Fiz. **47**, 1515 (1964); Sov. Phys. JETP **20**, 1018 (1965).

399 ² M. Brandbyge, J.-L. Mozos, P. Ordejón, J. Taylor, and K. Stokbro, Phys. Rev. B **65**, 165401
400 (2002).

401 ³ S. Sanvito, C.J. Lambert, J.H. Jefferson, A.M. Bratkovsky, Phys. Rev. B **59**, 11936 (1999).

402 ⁴ J. Taylor, H. Guo, and J. Wang, Phys. Rev. B **63**, 245407 (2001).

403 ⁵ Y. Xue, S. Datta, and M.A. Ratner, Chem. Phys. **281**, 151 (2002).

404 ⁶ J.R. Chelikowsky, N. Troullier, and Y. Saad, Phys. Rev. Lett. **72**, 1240 (1994); J.R. Chelikowsky,
405 N. Troullier, K. Wu, and Y. Saad, Phys. Rev. B **50**, 11355 (1994).

406 ⁷ T. Ono and K. Hirose, Phys. Rev. Lett. **82**, 5016 (1999); Phys. Rev. B **72**, 085115 (2005); T.
 407 Ono, M. Heide, N. Atodiresei, P. Baumeister, S. Tsukamoto, and S. Blügel, Phys. Rev. B **82**,
 408 205115 (2010).

409 ⁸ K. Hirose, T. Ono, Y. Fujimoto, and S. Tsukamoto, *First Principles Calculations in Real-Space*
 410 *Formalism, Electronic Configurations and Transport Properties of Nanostructures* (Imperial
 411 College, London, 2005).

412 ⁹ N.D. Lang, Phys. Rev. B **52**, 5335 (1995).

413 ¹⁰ N. Kobayashi, M. Brandbyge, and M. Tsukada, Phys. Rev. B **62**, 8430 (2000).

414 ¹¹ S. Tsukamoto and K. Hirose, Phys. Rev. B **66**, 161402 (2002).

415 ¹² H.J. Choi and J. Ihm, Phys. Rev. B **59**, 2267 (1999).

416 ¹³ K. Hirose and M. Tsukada, Phys. Rev. B **51**, 5278 (1995).

417 ¹⁴ Y. Fujimoto and K. Hirose, Phys. Rev. B **67**, 195315 (2003).

418 ¹⁵ S.H. Vosko, L. Wilk, and M. Nusair, Can. J. Phys. **58**, 1200 (1980); J.P. Perdew and A. Zunger,
 419 Phys. Rev. B **23**, 5048 (1981).

420 ¹⁶ J.P. Perdew, Phys. Rev. Lett. **55**, 1665 (1985); J.P. Perdew, J.A. Chevary, S.H. Vosko, K.A.
 421 Jackson, M.R. Pederson, D.J. Singh, and C. Fiolhais, Phys. Rev. B. **46**, 6671 (1992); J.P.
 422 Perdew, K. Burke and M. Ernzerhof, Phys. Rev. Lett. **77**, 3865 (1996); *ibid.* **78**, 1396 (1997).

423 ¹⁷ P. Hohenberg and W. Kohn, Phys. Rev. **136**, B864 (1964).

424 ¹⁸ W. Kohn and L.J. Sham, Phys. Rev. **140**, A1133 (1965).

425 ¹⁹ T. Ono and K. Hirose, Phys. Rev. B **70**, 033403 (2004).

426 ²⁰ A.R. Williams, P.J. Feibelman, and N.D. Lang, Phys. Rev. B **26**, 5433 (1982).

427 ²¹ M.P. López Sancho, J.M. López Sancho, and J. Rubio, J. Phys. F **14**, 1205 (1984); **15**, 851
 428 (1985).

429 ²² F. Guinea, C. Tejedor, F. Flores, and E. Louis, Phys. Rev. B **28**, 4397 (1983).

430 ²³ T. Ando, Phys. Rev. B **44**, 8017 (1991).

431 ²⁴ D.H. Lee and J.D. Joannopoulos, Phys. Rev. B **23**, 4997 (1981).

432 ²⁵ F. García-Moliner and V.R. Velasco, *Theory of Single and Multiple Interfaces*, (World Scientific,
 433 Singapore, 1992).

434 ²⁶ Y. Egami, K. Hirose, and T. Ono, Phys. Rev. E **82**, 056706 (2010).

435 ²⁷ P.A. Khomyakov, G. Brocks, V. Karpan, M. Zwierzycki, and P.J. Kelly, Phys. Rev. B **72**,
 436 035450 (2005).

- 437 ²⁸ M. Büttiker, Y. Imry, R. Landauer, and S. Pinhas, Phys. Rev. B **31**, 6207 (1985).
- 438 ²⁹ D.S. Fisher and P.A. Lee, Phys. Rev. B **23**, R6851 (1981).
- 439 ³⁰ We used the norm-conserving pseudopotentials NCPS97 constructed by K. Kobayashi using the
440 procedure proposed in Ref. 31. See K. Kobayashi, Comput. Mater. Sci. **14**, 72 (1999).
- 441 ³¹ N. Troullier and J. L. Martins, Phys. Rev. B **43**, 1993 (1991).
- 442 ³² L. Kong, J.R. Chelikowsky, J.B. Neaton, and S.G. Louie, Phys. Rev. B **76**, 235422 (2007).
- 443 ³³ V. Zólyomi and J. Kúrti, Phys. Rev. B **70**, 085403 (2004).

444 **FIGURES**

445

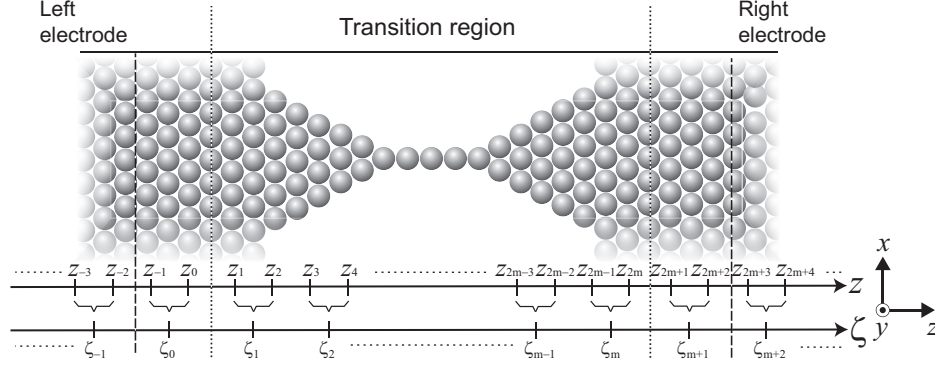


FIG. 1. Sketch of a system with the transition region intervening between the left and right semi-infinite crystalline electrodes. The dashed lines correspond to the borders of the partitioning of the Hamiltonian matrix in Eq. (1) and Fig. 2, whereas the dotted lines denote the borders of individual regions used in wave-function matching.¹⁴ The case for $\mathcal{N}_f = 2$ and $N_z = 2m$ is illustrated as an example, where \mathcal{N}_f corresponds to the order of the finite-difference approximation for the kinetic energy operator.

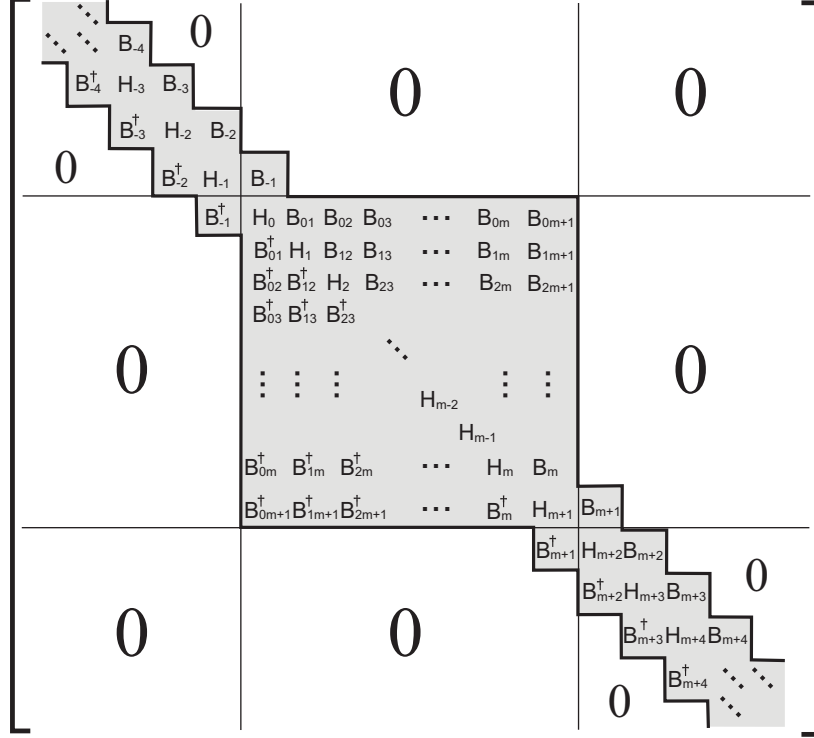


FIG. 2. Partitioning of the Hamiltonian matrix \hat{H} of Eq. (1), associated with the whole system sketched in Fig. 1. Block-matrix elements H_l, B_l and $B_{ll'}$ are the abbreviations of $H(\zeta_l, \mathbf{k}_{||})$, $B(\zeta_l)$ and $B(\zeta_l, \zeta_{l'})$, respectively. The partition lines are identical to those in Eq. (1).

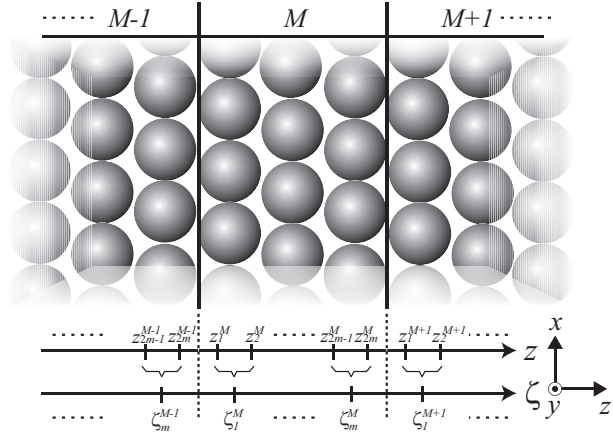


FIG. 3. Schematic representation of the periodic bulk. ζ_k^M represents the z -coordinate at the k th grid plane group in the M th unit cell.

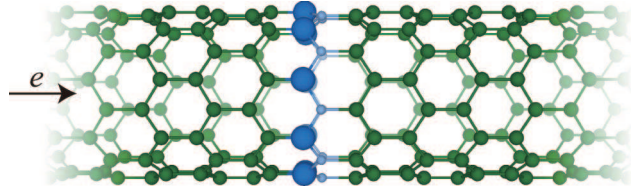


FIG. 4. (color online) Computational model where one BN zigzag ring is sandwiched between (9,0) CNT electrodes. Large dark, small dark, and small light balls are N, C, and B atoms, respectively. The rectangle enclosed by broken lines represents the supercell used to evaluate the optimized atomic configuration and Kohn-Sham effective potential.

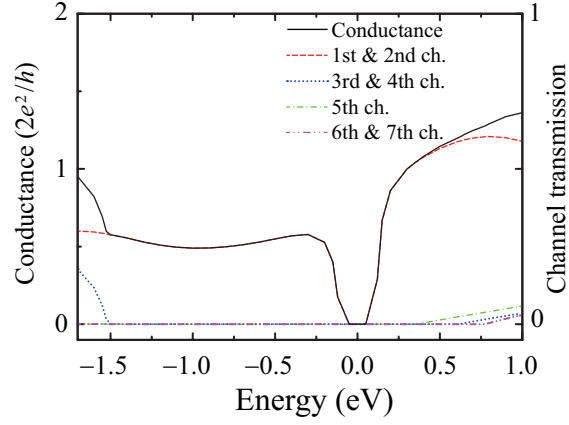


FIG. 5. Conductance spectra of C/BNNT as functions of energy of incident electrons. The solid curve represents conductance. Dashed, dotted, dash-dotted, and dashed double-dotted curves show channel transmissions.

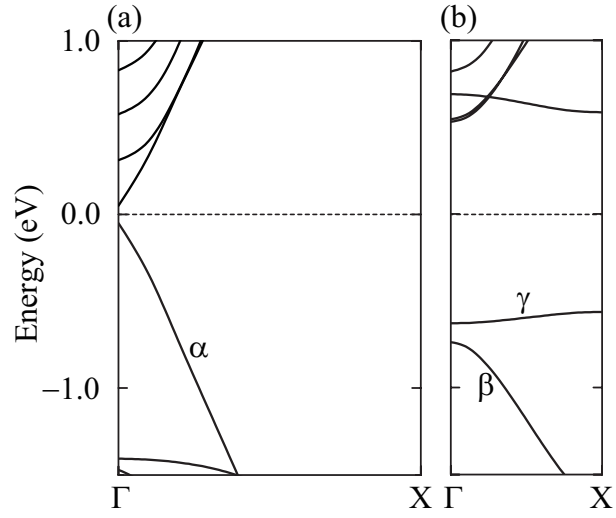


FIG. 6. Electronic band structures of (a) CNT and (b) C/BNNT. The supercells include two and four (9,0) rings for CNT and C/BNNT, respectively. The zero of energy is the Fermi energy.

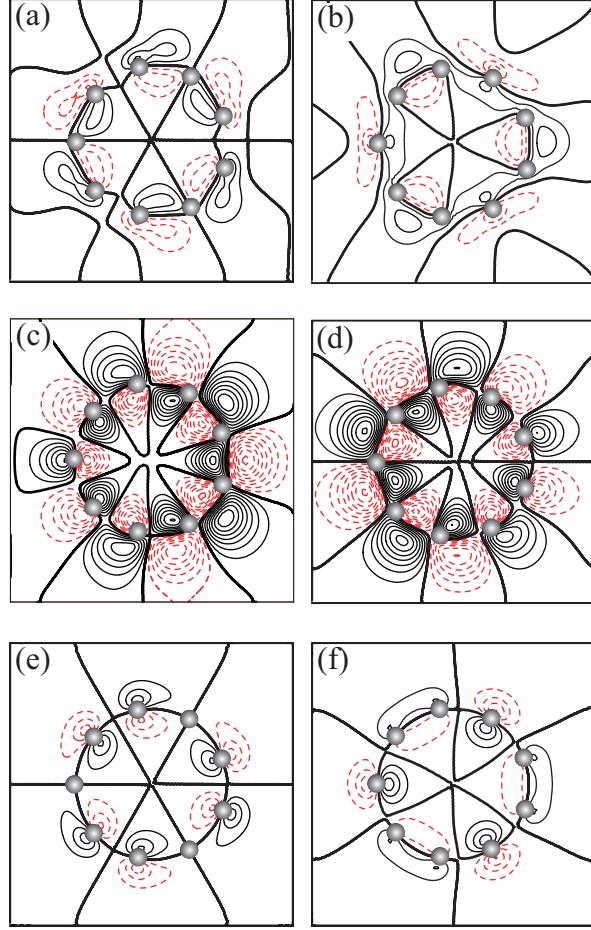


FIG. 7. Contour plots of wave functions. (a) and (b) Doubly degenerate bands indicated by β of C/BNNT in Fig. 6. (c) and (d) Doubly degenerate bands indicated by γ of C/BNNT. (e) and (f) Doubly degenerate bands indicated by α of CNT. Negative values are indicated by dashed curves; the thick solid curve represents zero. The contour plot is separated by 7.41×10^{-4} electron/ \AA^3 . The spheres represent the position of carbon atoms.

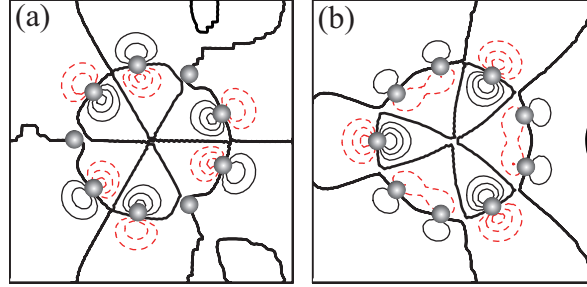


FIG. 8. Contour plots of doubly degenerate scattering wave functions at energy of $E_F - 0.5$ eV. Negative values are indicated by dashed curves; the thick solid curve represents zero. The contour plot is separated by 3.27×10^{-4} electron/ $\text{\AA}^3/\text{eV}$. The spheres represent the position of carbon atoms.